Performance Analysis in Serial-section Electron Microscopy Image Registration of Neuronal Tissue

Bohao Chen[a,b], Tong Xin[a,b], Hua Han[a,c,d,e], and Xi Chen[a]

[a]Institute of Automation, Chinese Academy of Sciences, Beijing, China
[b]School of Artificial Intelligence, University of Chinese Academy of Sciences, Beijing, China
[c]The Center for Excellence in Brain Science and Intelligence Technology, CAS, Shanghai, China
[d]National Laboratory of Pattern Recognition, CASIA, Beijing, China
[e]School of Future Technology, University of Chinese Academy of Sciences, Beijing, China

ABSTRACT

Serial-section electron microscopy is a widely used technique for neuronal circuit reconstruction. However, the continuity of neuronal structure is destroyed when the tissue block is cut into a series of sections. The neuronal morphology in different sections changes with their locations in the tissue block. These content changes in adjacent sections bring a difficulty to the registration of serial electron microscopy images. As a result, the accuracy of image registration is strongly influenced by neuronal structure variation and section thickness.

To evaluate registration performance, we use the spherical deformation model as a simulation of the neuron structure to analyze how registration accuracy is affected by section thickness and neuronal structure size. We mathematically describe the trend that the correlation of neuronal structures in two adjacent sections decreases with section thickness. Furthermore, we demonstrate that registration accuracy is negatively correlated with neuronal structure size and section thickness by analyzing the second-order moment of estimated translation. The experimental results of registration on synthetic data demonstrate that registration accuracy decreases with the neuronal structure size.

Keywords: Registration accuracy, Serial section, Neuronal structure, Spherical deformation model

1. INTRODUCTION

Serial-section electron microscopy (ssEM) is a well-established imaging technique that has been widely used in neuronal circuits reconstruction.[1–4] Brain tissue is fixed in resin, sliced into a series of ultrathin sections, and finally imaged by electron microscopy to obtain images of neural tissue sections at nanoscale resolution.[5] However, due to the slicing process, the spatial continuity of the neuronal structures is disrupted. To solve this problem, the registration process is introduced before volume reconstruction. By performing a linear or nonlinear transformation on the sections, registration restores the spatial continuity of the neuronal structures and facilitates subsequent reconstruction.

Since the tissue block is cut into a series of sections, the content in different sections changes with their Z-axis locations in the block, which means the neuronal morphology in adjacent sections is similar but isn't precisely the same.[2,6,7] And, an intuitive understanding is that the thicker the section is, the further apart the adjacent images are in Z-axis, and the more significant the difference in their content. These structural changes in adjacent sections bring difficulty to the registration of ssEM images, which is necessary to recover the continuity of neuronal structure. As a result, the image registration accurary is strongly influenced by neuronal structure variation and section thickness.

Previous registration performance analysis focus on the relation between registration accuracy and image noise.[8–10] However, the main factor affecting accuracy in ssEM image registration is structural variation related to the image content and cannot be represented by Gaussian noise.[7] Figure 1 shows the comparison between noise-contaminated image and actual source image in ssEM image registration. Previous work divided the deformation patterns in electron microscopy (EM) images of biological tissue into shape, texture, and quantity variability.[11] In this paper, we focus on the registration accuracy with the shape variation of a single neuronal

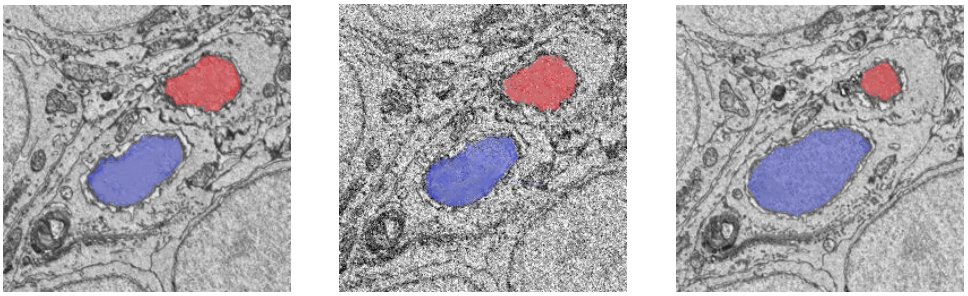

(a) (b) (c)

Figure 1. Comparison of noise-contaminated images and actual source images in ssEM image registration. (a) Template ssEM image. (b) shows the template image contaminated by Gaussian noise. The relationship between noise and registration accuracy based on this noise image model had been analyzed in previous work. (c) Actual adjacent ssEM image of (a). Red and blue mark the two neuronal structures in the ssEM images, respectively.

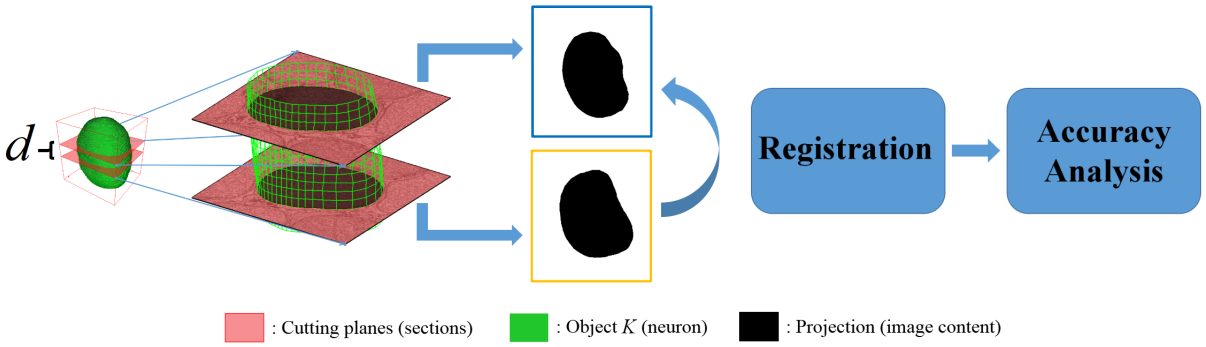

Figure 2. Illustration of registration model and further process. We use a structure described by the 3-dimensional shape model (left) to simulate the morphological change of neuronal structure in adjacent sections. The neuronal structure projections on images are regarded as the content of images to be aligned (middle). We register these two images and analyze the registration accuracy (right). The section thickness is denoted as d.

structure. More specifically, we mathematically analyze the registration accuracy with the size of neuronal structure and the section thickness. Our analysis provides a theoretical basis for the future improvement of ssEM image registration.

2. METHOD

The neuronal structures acquired from reconstruction suffer from section stretching, distorting, and artifacts individually during section preparation, imaging and registration. To get around the difficulty of getting accurate neuronal structure, we use a shape model to generate a 3-dimensional object K as a neuron in biological tissue. This object K is cut by two parallel planes with distance d. These cutting planes are regarded as different sections in neuronal circuit reconstruction. And d is regarded as section thickness. The projections of K on the cutting planes are considered as content on images to be registered. We register these two images and then analyze the relationship between the section thickness d and neuron size. Figure 2 illustrates our registration model and further process.

2.1 The Spherical Deformation Model

Before we analyze the factors affecting the accuracy of ssEM image registration, we first introduce the spherical deformation model,[12] which is used to simulate neurons in this paper. For a 3-dimensional sphere-shaped object

K, this model selects a point $z \in K$ as origin and describes the surface of K by spherical coordinates as $\{z + r(\theta,\phi)\omega(\theta,\phi) : 0 \le \theta < 2\pi, 0 \le \phi \le \pi\}$, where $\omega(\theta,\phi) = (\cos\theta\sin\phi,\ \sin\theta\sin\phi,\ \cos\phi)$ is the vector on the unit sphere with polar longitude θ and polar latitude ϕ, and $r(\theta,\phi)$ is the distance from z to the surface of K. In the following sections, we consider the standardized radius $r(\theta,\phi)/\bar{r}$, where $\bar{r}$ is the mean radius length. The standardized radius function is written as

$$r(\theta,\phi) = 1 + \sum_{n=2}^{\infty}\sum_{m=-n}^{n} a_n^m \varphi_n^m(\theta,\phi), \tag{1}$$

where $\varphi_n^m(\theta,\phi)$ is the spherical harmonic function. The spherical harmonics are given by

$$\varphi_n^m(\theta,\phi) = \begin{cases} k_n^{|m|} P_n^{|m|}(\cos\phi)\cos m\theta, & m = -n,\dots,-1 \\ k_n^0 P_n^0(\cos\phi), & m = 0 \\ k_n^m P_n^m(\cos\phi)\sin m\theta, & m = 1,\dots,n, \end{cases}$$

where k_n^m is normalizing constant, and P_n^m is the associated Legendre function of the first kind. In the standardized radius function, each spherical harmonic function has a coefficient a_n^m, modeled as independent Gaussian random variables submitted to $\mathcal{N}(0,\lambda_n^m)$. The surface of K is supposed to be stationary, and stationarity is obtained by assuming $\lambda_n^m = \lambda_n,\ n \ge 2,\ m = -n,\dots,n$. We also assumed that the variance λ_n decrease according to

$$\begin{aligned} 1/\lambda_n &= \alpha + \beta(n^p - 2^p), \\ n \ge 2,\ p > 2,\ \alpha,\ \beta &> 0. \end{aligned} \tag{2}$$

The pre-defined parameter p determines the smoothness of K, while the other two pre-defined parameters α and β determine the global and local shape, respectively. More information about the spherical deformation model can be found in 12.

2.2 Correlation of Shapes in Adjacent Sections

In this subsection, we focus on the correlation of two radius r_i at different polar latitudes ϕ_i, $i = 1, 2$. With stationarity on K, the covariance of lengths of two points $r(\theta_1,\phi_1)$ and $r(\theta_2,\phi_2)$, depends on the angle ψ between two points as following,

$$\mathrm{Cov}(r(\theta_1,\phi_1), r(\theta_2,\phi_2)) = \sum_{n=2}^{\infty}\lambda_n \sum_{m=-n}^{n} \varphi_n^m(\theta_1,\phi_1)\varphi_n^m(\theta_2,\phi_2) = \sum_{n=2}^{\infty}\lambda_n (k_n^0)^2 P_n(\cos\psi),$$

where $\cos\psi = \omega(\theta_1,\phi_1)\cdot\omega(\theta_2,\phi_2)$, and $P_n = P_n^0$. The ψ represents the angle between two points on the surface. Figure 3 (a) shows the angle ψ of two radius vectors, and figure 3 (b) shows the covariance function and weighted legendre functions with $\psi \in [0,\pi/2]$. We firstly consider the correlation between two radius r_i at different longitudes ϕ_i with same latitude θ, which is corresponding to the correlation of same local structures in adjacent sections. The covariance function becomes

$$\mathrm{Cov}(r(\theta,\phi_1), r(\theta,\phi_2)) = \sum_{n=2}^{\infty}\lambda_n (k_n^0)^2 P_n(\cos\Delta\phi), \tag{3}$$

where $\Delta\phi = \phi_1 - \phi_2$, as figure 3 (c) shows. With pre-defined parameters (α,β,p), the covariance function depends on $\Delta\phi$ now. In the ssEM image registration, $\sin(\Delta\phi/2)$ equals the ratio of half of section thickness d to the mean radius $\bar{r}$ of the neuronal structure, that is, $\Delta\phi = 2\arcsin(d/2\bar{r})$. Since in neuronal circuit reconstruction, researchers use ultra-thin sections to reconstruct neuronal structure,[13] we assume d is less than $\sqrt{2}$ times of mean radius $\bar{r}$, which makes $\Delta\phi \in [0,\pi/2)$, and $\sin\Delta\phi$ is a monotonic increasing function with $\Delta\phi \in [0,\pi/2)$. Figure 3 (d) shows the change of the covariance with thickness d. The above analysis describes the correlation of a single point on the neuronal structure contour in adjacent sections with the section thickness d. When this correlation is extended from a single point to the whole structure contour by $\theta = [0, 2\pi)$, the covariance function mathematically describes the phenomenon that the correlation of neuronal structure in adjacent sections decreases with section thickness d.

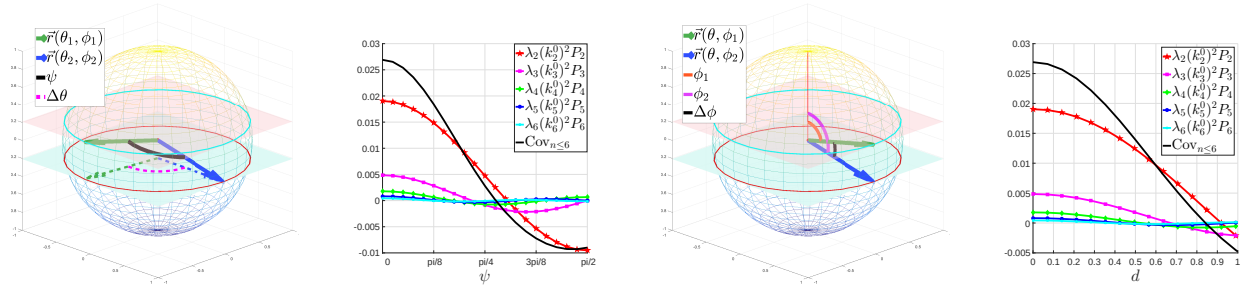

(a) (b) (c) (d)

Figure 3. (a) The angle ψ and the angle $\Delta\theta$ of two radius vectors. $\Delta\theta = \theta_1 - \theta_2$, which means the difference of longitude θ of two vectors. (b) The covariance function with $n \leq 6$ and the weighted legendre functions, with $\psi \in [0, \pi/2]$. $(\alpha, \beta, p) = (20.2, 0.9, 4.4)$. The exponential decay characteristic of λ_n in equation (2) enables the covariance to be approximated by the first few terms. (c) The angle $\Delta\phi$ of two radius vectors at same θ. (d) The figure shows the correlation decrease with the increase of section thickness d. For the covariance function and the weighted legendre functions, we fix the mean radius $\bar{r} = 1$ and change d from 0 to 1.

2.3 Registration Accuracy Analysis

Since the translation-only registration is widely needed in ssEM image registration,[5,7,14] in this subsection, we focus on the translation-only registration where two images to be aligned with different cross-sections of object K, which the spherical deformation model describes.

We consider two images S and T, representing the source image and target image, respectively. The true translation between two images is denoted as $(\Delta t, \Delta s)$. In registration, we first extract N corresponding landmarks $l_i = (x_i, y_i)$ in image S and T. Next, we estimate the translation based on the given cost function. The cost function is as following,

$$\sum_{i=1}^{N}(x_{iT} - (x_{iS} + u))^2 + (y_{iT} - (y_{iS} + v))^2, \tag{4}$$

where u and v are the translation in X-axis and Y-axis, respectively. We align image S and T by estimating the translation $(\widehat{\Delta t}, \widehat{\Delta s})$, which minimizes the cost function. To minimize the effect of morphological variation on registration, we select a center inside the structure and sample N landmarks on the contour at equal angular intervals. Since we consider translation-only registration, landmark l_{iT} in T is corresponding to landmark l_{iS} in S, which are both sampled at same θ_i.

We use ρ_{ik} to represent distance from origin to the ith landmark l_{ik} sampled at θ_i in image k, $k = \{S, T\}$. ρ_i is actually the projection of unnormalized radius-vector on the cutting plane. Thus, $\rho_{ik} = r(\theta_i, \phi_k)\bar{r}\sin\phi_k$. We use the mean radius length $\bar{r}$ to represent the neuronal structure size. Since researchers use ultra-thin sections in neuronal circuit reconstruction, the size of neuronal structures in adjacent sections are assumed to be the same. That is, the mean distance $\bar{\rho}_T$ from the origin to the contour of the neuronal structure in T is assumed to be the same with the mean distance $\bar{\rho}_S$ in S. This relation can be written as $E(\rho_{iT}) \approx E(\rho_{iS})$, and can be simplified to $\sin\phi_T \approx \sin\phi_S$. In our experiments, we suppose $\sin\phi_T = \sin\phi_S = \sin\phi$.

By computing the partial derivative of the cost function with respect to u and making the derivative function be zero, we get

$$\begin{aligned}\widehat{\Delta t} =& \frac{1}{N}\sum_{i=1}^{N}(x_{iT} - x_{iS}) = \frac{1}{N}\sum_{i=1}^{N}(\bar{x}_T + \rho_{iT}\cos\theta_i - \bar{x}_S - \rho_{iS}\cos\theta_i) \\ =& \Delta t + \frac{\bar{r}\sin\phi}{N}\sum_{i=1}^{N}\cos\theta_i(r_{iT} - r_{iS}) \ ,\end{aligned}$$

where $\bar{x}_k$ is X-axis coordinate of the origin in image k, and $\bar{x}_T = \bar{x}_S + \Delta t$. The second-order moment of $(\widehat{\Delta t} - \Delta t)$ is as following,

$$\begin{aligned} E\left((\widehat{\Delta t} - \Delta t)^2\right) =& \frac{\bar{r}^2(\sin\phi)^2}{N^2} E\left(\sum_{i=1}^{N}\sum_{j=1}^{N} \cos\theta_i \cos\theta_j (r_{iT} - r_{iS})(r_{jT} - r_{jS})\right) \\ =& \frac{\bar{r}^2(\sin\phi)^2}{N^2} \sum_{i=1,j=1}^{N} 2\cos\theta_i \cos\theta_j (\mathrm{Cov}_{iTjT} - \mathrm{Cov}_{iSjT}) \ , \end{aligned} \tag{5}$$

where $\mathrm{Cov}_{ik_1jk_2} = \mathrm{Cov}(r(\theta_i, \phi_{k_1}), r(\theta_j, \phi_{k_2}))$. Equation (5) shows that $E((\widehat{\Delta t} - \Delta t)^2)$ is proportional with $\bar{r}^2$, which means the registration accuracy is negatively correlated with neuronal structure size. Meanwhile, we have

$$\begin{aligned} \mathrm{Cov}_{iTjT} - \mathrm{Cov}_{iSjT} =& \sum_{n=2}^{\infty} \lambda_n (k_n^0)^2 \left(P_n(\cos\Delta\theta_{ij}) - P_n(\cos\psi_{ij})\right) \\ =& \sum_{n=2}^{\infty} \lambda_n (k_n^0)^2 \dot{P}_n(\delta_n)(\cos\Delta\theta_{ij} - \cos\psi_{ij}) \\ =& \frac{d^2}{4\bar{r}^2} \sum_{n=2}^{\infty} \lambda_n (k_n^0)^2 \dot{P}_n(\delta_n)(1 + \cos\Delta\theta_{ij}) \ , \end{aligned} \tag{6}$$

where $\dot{P}_n$ is the derivative function of P_n, and $\delta_n \in [p_n, q_n], p_n = \min(\cos\psi_{ij}, \cos\Delta\theta_{ij}),\ q_n = \max(\cos\psi_{ij}, \cos\Delta\theta_{ij})$. The last equation uses the cosine-formula.[15] Equation (6) shows that $(\mathrm{Cov}_{iTjT} - \mathrm{Cov}_{iSjT})$ is positively correlated with d. Thus, $E((\widehat{\Delta t} - \Delta t)^2)$ is positively correlated with d, which means $\widehat{\Delta t}$ is more inaccurate with the increase of section thickness. The above analysis is same to $\widehat{\Delta s}$ in Y-axis.

Consider selecting a point inside the neuronal structure as the origin. An ideal origin needs to be unaffected by structural deformation and only responds to the translation of neuronal structure. Center of mass might be a possible option. It can remain stable when the shape of the neuronal structure is slightly deformed. Moreover, it is easy to calculate the center of mass. Next, we analyze how accurately the center of mass is positioned with respect to the ground truth center.

We set the ground truth center, which is actually the projection of origin z in section 2.1, as $(0, 0)$ and calculate the center of mass (x_c, y_c) in this coordinate system. The X-axis coordinate of center of mass can be written as $x_c = \frac{1}{M}\iint_P x\mathrm{d}x$, where P is the projection of K on the cutting plane and M is the area of P. M can be calculated by integrating over the whole structure, $M = \iint_P \mathrm{d}x\mathrm{d}y$. We use $E(M) = \pi\bar{r}^2\sin^2\phi$ instead of M to reduce the computational complexity. And we have

$$\begin{aligned} \frac{1}{E(M)} \iint_P x\mathrm{d}x =& \frac{1}{3E(M)} \int_0^{2\pi} \rho^3(\theta, \phi)\cos\theta \mathrm{d}\theta \\ \approx& \frac{2\pi}{3NE(M)} \sum_{n=1}^{N} \rho^3(\theta_n, \phi)\cos\theta_n \\ =& \frac{2\pi\bar{r}^3\sin^3\phi}{3NE(M)} \sum_{n=1}^{N} \left(1 + \sum_{i=2}^{\infty}\sum_{j=-i}^{i} a_i^j \psi_i^j(\theta_n, \phi)\right)^3 \cos\theta_n \\ \approx& \frac{2\bar{r}\sin\phi}{N} \sum_{n=1}^{N}\sum_{i=2}^{\infty}\sum_{j=-i}^{i} a_i^j \psi_i^j(\theta_n, \phi)\cos\theta_n \ . \end{aligned} \tag{7}$$

The last equation is derived using Taylor expansion and discarding high-order terms. We can estimate $E(x_c^2)$ as follows,

$$E(x_c^2) \approx \frac{4\bar{r}^2 \sin^2\phi}{N^2} \sum_{i=2}^{\infty} \lambda_i \sum_{j=-i}^{i} \sum_{n=1}^{N} \left(\psi_i^j(\theta_n, \phi)\cos\theta_n\right)^2 . \tag{8}$$

Equation (8) demonstrates that the accuracy of estimate of centre of mass to ground truth center is negatively correlated with $\bar{r}$. This relation may suggest extracting the centers of mass on small neural structures to improve registration accuracy.

3. RESULTS

In this section, we first design an experiment to demonstrate that the accuracy of center of mass is negatively correlated with $\bar{r}$. In figure 4(a), we illustrate the distribution of centers of mass at different $\bar{r}$. Figure 4(b) and (c) compare the experimental results $E(x_c^2)$ and $E(y_c^2)$ with our theoretical prediction by equation (8).

Next we design an experiment to verify equation (5). We generate a set of section neuronal structure shape data based on the deformation model. It contains 24 subsets with different $\bar{r}$ and each subset contains 1000 pairs of target image T and source image S, $\bar{r} = \{25, 50, 75, \ldots, 600\}$ pixels. The section thickness d is set to 40 pix in all subsets. $(\Delta t, \Delta s)$ =(4.5 pixels, 4.5 pixels). The model parameters we used are $(\alpha, \beta, p) = (20.2, 0.9, 4.4)$, which is calculated by fitting neurons in human brain.[12]

For a pair of T and S, we first select origins and sample points at a pre-defined angular interval on the contours. We use centers of mass and ground truth centers as origins to compare the influence of origin on registration accuracy. And we extract landmarks from accurate contours and discrete images to compare the influence of discrete samples. The angular interval is $\pi/50$. Secondly, we calculate $\widehat{\Delta t}$ and $\widehat{\Delta s}$ by the derivative function of the cost function. Finally we calculate the second-order moment of $(\widehat{\Delta t} - \Delta t)$ and $(\widehat{\Delta s} - \Delta s)$ among the subset of same $\bar{r}$. The calculated second-order moments are compared with the prediction of equation (5) to verify our analysis.

Figure 5 illustrates experimental results. The results obtained from the ground truth center are generally consistent with our predictions. The experimental results also show that the second-order moments of estimated translation with the center of mass grow in the same trend as predicted. However, there is a gap between the results obtained from the center of mass and our prediction. Comparing the results using only the center of mass shows that this gap is caused by the inaccurate positioning of the center of mass to the ground truth center. Our results also illustrate that whether the landmarks are sampled from the accurate contours does not significantly affect the registration accuracy.

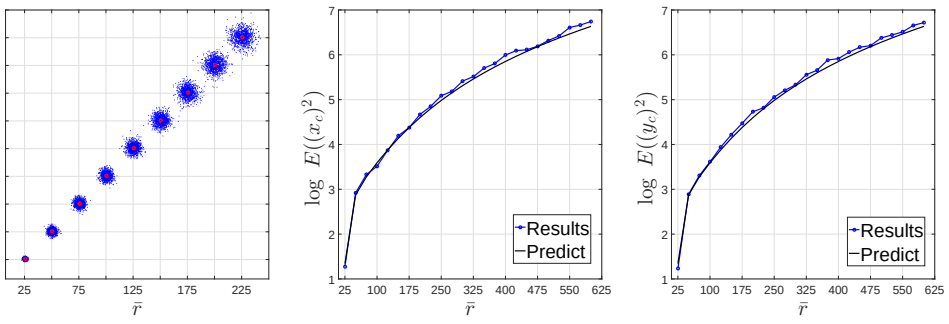

(a) (b) (c)

Figure 4. (a) illustrates distribution of the centers of mass at different $\bar{r}$. The red points are regarded as $(0, 0)$ for its surronding samples. (b) compares the results of $E(x_c^2)$ and (c) compares the results of $E(y_c^2)$ with theoretical prediction.

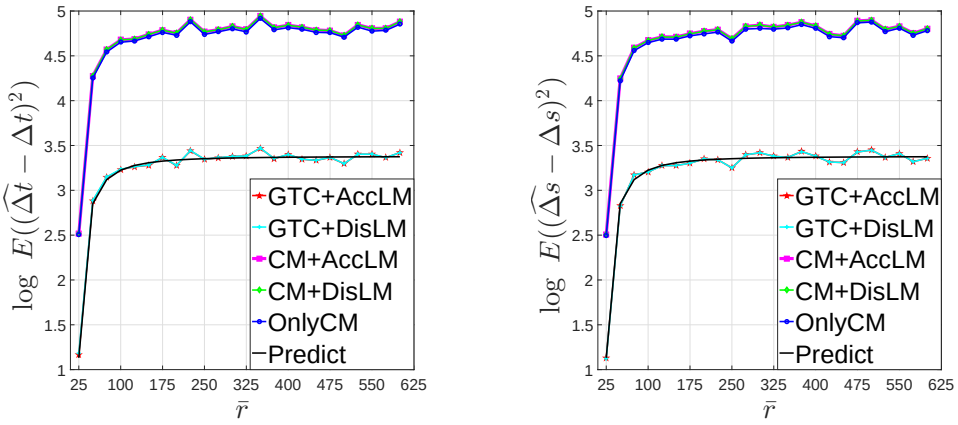

(a) (b)

Figure 5. (a) compares the results of the logarithm of the second-order moment of $(\widehat{\Delta t}-\Delta t)$ and (b) compares the results of $(\widehat{\Delta s}-\Delta s)$ with the theoretical prediction. GTC: Registration uses the ground truth center as the origin. CM: Registration uses the center of mass as the origin. AccLM: Landmarks are extracted from accurate contours. DisLM: Landmarks are extracted from discrete image contours. OnlyCM: Registration only uses the center of mass to register two images, which is used to compare different origins' influence.

4. CONCLUSION

In this paper, by using the spherical deformation model to simulate neuronal structures in ssEM images, we mathematically describe the trend that the correlation of neuronal structure in adjacent sections decreases with section thickness. Furthermore, we analyze the relationship between registration accuracy and section thickness as well as neuronal structure size. Our analysis shows that the second-order moment of the estimated translation increase with mean radius length $\bar{r}$. The experimental results on the synthetic data sets effectively support our analysis.

ACKNOWLEDGMENTS

The authors would like to thank the Strategic Priority Research Program of Chinese Academy of Science (No. XDB32030200, No. XDA27010403), Instrument Function Development Innovation Program of Chinese Academy of Sciences (No. E0S92308) and CAS Key Technology Talent Program (No. 292019000126) for the financial support.

REFERENCES

[1] Witvliet, D., Mulcahy, B., Mitchell, J. K., Meirovitch, Y., Berger, D. R., Wu, Y., Liu, Y., Koh, W. X., Parvathala, R., Holmyard, D., et al., "Connectomes across development reveal principles of brain maturation," *Nature* , 1–5 (2021).

[2] Phelps, J. S., Hildebrand, D. G. C., Graham, B. J., Kuan, A. T., Thomas, L. A., Nguyen, T. M., Buhmann, J., Azevedo, A. W., Sustar, A., Agrawal, S., et al., "Reconstruction of motor control circuits in adult drosophila using automated transmission electron microscopy," *Cell* **184**(3), 759–774 (2021).

[3] Motta, A., Berning, M., Boergens, K. M., Staffler, B., Beining, M., Loomba, S., Hennig, P., Wissler, H., and Helmstaedter, M., "Dense connectomic reconstruction in layer 4 of the somatosensory cortex," *Science* **366**(6469) (2019).

[4] Hildebrand, D. G. C., Cicconet, M., Torres, R. M., Choi, W., Quan, T. M., Moon, J., Wetzel, A. W., Champion, A. S., Graham, B. J., Randlett, O., et al., "Whole-brain serial-section electron microscopy in larval zebrafish," *Nature* **545**(7654), 345–349 (2017).

[5] Saalfeld, S., Fetter, R., Cardona, A., and Tomancak, P., "Elastic volume reconstruction from series of ultra-thin microscopy sections," *Nature methods* **9**(7), 717–720 (2012).

[6] Zheng, Z., Lauritzen, J. S., Perlman, E., Robinson, C. G., Nichols, M., Milkie, D., Torrens, O., Price, J., Fisher, C. B., Sharifi, N., et al., "A complete electron microscopy volume of the brain of adult drosophila melanogaster," *Cell* **174**(3), 730–743 (2018).

[7] Wetzel, A. W., Bakal, J., Dittrich, M., Hildebrand, D. G., Morgan, J. L., and Lichtman, J. W., "Registering large volume serial-section electron microscopy image sets for neural circuit reconstruction using fft signal whitening," in [*2016 IEEE Applied Imagery Pattern Recognition Workshop (AIPR)*], 1–10, IEEE (2016).

[8] Robinson, D. and Milanfar, P., "Fundamental performance limits in image registration," *IEEE Transactions on Image Processing* **13**(9), 1185–1199 (2004).

[9] Uss, M. L., Vozel, B., Dushepa, V. A., Komjak, V. A., and Chehdi, K., "A precise lower bound on image subpixel registration accuracy," *IEEE transactions on geoscience and remote sensing* **52**(6), 3333–3345 (2013).

[10] Ketcha, M. D., De Silva, T., Han, R., Uneri, A., Goerres, J., Jacobson, M., Vogt, S., Kleinszig, G., and Siewerdsen, J. H., "Fundamental limits of image registration performance: effects of image noise and resolution in ct-guided interventions," in [*Medical Imaging 2017: Image-Guided Procedures, Robotic Interventions, and Modeling*], **10135**, 1013508, International Society for Optics and Photonics (2017).

[11] Miller, M. I., Joshi, S., Maffitt, D. R., Mcnally, J. G., and Grenander, U., "Membranes, mitochondria and amoebae: shape models," *Journal of Applied Statistics* **21**(1-2), 141–163 (1994).

[12] Hobolth, A., "The spherical deformation model," *Biostatistics* **4**(4), 583–595 (2003).

[13] Kornfeld, J. and Denk, W., "Progress and remaining challenges in high-throughput volume electron microscopy," *Current opinion in neurobiology* **50**, 261–267 (2018).

[14] Buniatyan, D., Popovych, S., Ih, D., Macrina, T., Zung, J., and Seung, H. S., "Weakly supervised deep metric learning for template matching," in [*Science and Information Conference*], 39–58, Springer (2019).

[15] Smart, W. M. and Green, R., [*Textbook on spherical astronomy*], Cambridge University Press (1977).